

Defects, parcellation, and renormalized negative diffusivities in non-homogeneous oscillatory media

Marie Sellier-Prono,¹ Massimo Cencini,² David Kleinfeld,^{3,4} and Massimo Vergassola^{1,3}

¹*Laboratoire de Physique, Ecole Normale Supérieure, CNRS,
PSL Research University, Sorbonne University, Paris 75005, France*

²*Istituto dei Sistemi Complessi, CNR, via dei Taurini 19,
00185 Rome, Italy and INFN, sez. Roma2 “Tor Vergata”*

³*Department of Physics, University of California, San Diego, La Jolla, CA 92093, USA*

⁴*Department of Neurobiology, University of California, San Diego, La Jolla, CA 92093, USA*

Coupling among oscillators in spatially-extended systems tends to lock their frequency at a common value. In the presence of spatial non-homogeneities, locking of different regions at different frequencies leads to parcellation, i.e., a series of synchronized clusters (plateaus). Motivated by rhythmic dynamics in physiological systems, we consider a Ginzburg-Landau (GL) model with a gradient of natural frequencies. We determine the scaling of the number of plateaus and their typical length *vs* dynamical parameters. Plateaus are separated by defects, where the amplitude of the GL field vanishes and phase differences are reset. For Dirichlet boundary conditions, we use asymptotic methods to determine the field profile around defects. For Neumann boundary conditions, we relate the stability phase diagram and defects’ precursors to the spectrum of the non-Hermitian Bloch-Torrey equation, originally introduced for nuclear magnetic resonance. In the non-linear regime, we trace the formation of defects to a non-linear renormalization of the diffusivity, which leads to spatially-modulated negative values and an instability that drives amplitude modulation.

Spatially-extended oscillations appear in a variety of situations, ranging from engineering to living, physical, and social systems [1–3]. Hallmarks of nonlinearities and spatial couplings that characterize those systems are synchronization among different oscillators, and entrainment by external forcing. Synchronization is the oscillation in unison of oscillators that in isolation have different frequencies yet lock because of their mutual coupling. A spectacular example is the synchronized flashing of thousands of firefly males during mating season [4, 5]. Other well-studied examples include locomotion, especially by fish [6], and electrical waves in neural computations [7, 8]. Entrainment by external forcing is the locking of oscillators to the driving rhythm. A physiological instance that impacts functional magnetic resonant imaging (fMRI) is vasomotion [9, 10]. Arterioles that source blood to the brain have the diameter of their walls driven by oscillations of the surrounding smooth muscle cells. In the presence of external neuronal stimuli, a strong vasomotion increase is observed at the drive frequency [11].

A number of theoretical methods have been developed to grasp the above phenomena. Phase models [1, 2] are rooted in the insight that weak couplings among oscillators perturb the stable limit cycle of each oscillator in a specific manner: Transverse perturbations relax rapidly, while phase perturbations along the cycle can be large and do not relax (zero modes). Technically, the limit cycle and its isochrones [12] are unperturbed, while weak perturbations drive the phase. The major simplification is that each oscillator is described by only a single variable, its phase in the limit cycle, rather than the original, generally multidimensional, description (see Supplementary Material [13] for their relationship). The famous

Kuramoto transition to synchronization [1] was obtained within this framework.

We focus on spatially non-homogeneous oscillatory media. Non-homogeneity may be caused by spatial variations of the parameters, e.g., the frequency of oscillators, or non-uniform external drive. Our motivation stems from two natural systems under intense experimental investigation: the aforementioned cortical vasomotion [9–11], and peristalsis [14, 15]. Interstitial cells in the small intestine of mammals bear spontaneous oscillations, which are synchronized by gap junction couplings, and generate rhythmic waves of contraction. Non-homogeneity is brought by the frequencies of the oscillators in isolation decreasing aborally in a roughly linear fashion from the stomach to the colon (see Fig. 1a), found by *post hoc* sectioning of the intestine [14]. In the intact intestine, couplings result in parcellation, i.e., a series of frequency plateaus as in Fig. 1a. Oscillations within the plateaus are regular, while their boundary displays “waxing and waning” (see Fig. 1b) that results from the interference of mismatched adjacent cell populations [14].

To understand parcellation, it is natural to consider a chain of weakly coupled oscillators with a gradient of natural frequencies. Ref. [16] pioneered this approach and demonstrated the existence of plateaus. However, as already noted in [17], the strong amplitude modulation at the boundary of plateaus is incompatible with the weak coupling approximation. A first alternative is to consider chains of nonlinear oscillators, *viz.*, van der Pol type [18, 19], which is relevant for density waves in dusty plasmas [20]. Numerical simulations confirmed the existence of plateaus and evidenced “oscillator death” for large enough gradients, i.e., the presence of regions with

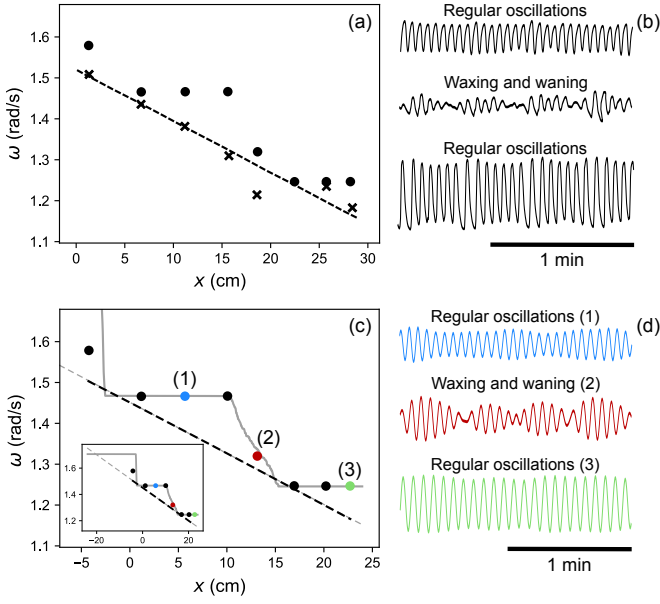


FIG. 1. (Color online) Comparison between experimental peristalsis and our GL modeling data. (a) Average frequencies recorded in isolated segments of cat intestine (crosses; the black dashed line is their linear fit) and in the intact intestine (circles); (b) Time-course signals in the bulk of two distinct plateaus (top and bottom), where relatively regular oscillations are observed, and in the region of “waxing and waning” in between. Data were extracted from figures in [14] as described in [13]. Panels (a) and (b) refer to two different experimental realizations so we do not associate the curves in (b) to specific points in (a). In panels (c) and (d) we show the same curves as in (a) and (b) obtained from our GL modeling with the use of the procedure detailed in [13]. The plateau architecture is captured, as well as the structure of the three time courses that we locate by their colors. The inset shows the full simulation domain.

oscillators unexcited [21–23]. A second alternative is to consider a Ginzburg-Landau (GL) model (see [24]) with a gradient of natural frequencies. The advantage is that the GL equation is the universal normal form close to a supercritical Hopf bifurcation. Oscillations are described by a complex field with a phase as well as an amplitude, contrary to phase models. Refs. [17, 25, 26] numerically demonstrated plateaus in the GL equation and analyzed its full locking and oscillator death at large gradients. In the GL formulation, the “waxing and waning” at the boundary of plateaus is associated to defects, i.e., locations where the amplitude of the complex field vanishes at specific times and its phase is thus undefined [2].

Here, we shall revisit the GL equation with a gradient of natural frequencies to provide insight into the formation and properties of plateaus, as well as the dynamics at high gradients. Specifically, we determine the scaling of length and number of plateaus, and calculate by asymptotic analysis the field profile in the region around a defect. For strong gradients, we identify the stability chart of the oscillator death state. In the nonlinear

regime, we derive that non-linear renormalization of the diffusivity yields negative values that destabilize full locking and drive amplitude modulation and defects. Finally, we show that the experimental curves in Fig. 1 are captured by a GL model with an additional advective term.

We consider a one-dimensional Ginzburg-Landau (GL) equation for the complex field $A(x, t)$:

$$\partial_t A(x, t) = rA(1 - |A|^2) + igx A + D\Delta A, \quad (1)$$

which is the Stuart-Landau normal form for oscillators close to a supercritical Hopf bifurcation, with diffusion accounting for spatial local couplings [1, 2]. We rescaled the amplitude of A to match the cubic and the instability coefficient, $r > 0$, which we take real, along with taking D as real and positive. These assignments are justified *a posteriori* by the agreement with data in Fig. 1. Note that the cubic nonlinearity is dictated by gauge invariance under $A \mapsto Ae^{i\phi}$. The linear gradient $\omega(x) = gx$ introduces spatial non-homogeneity. It also breaks parity, which allows *a priori* for an additional term $\propto \nabla A$ that we shall consider later.

A straightforward means to demonstrate parcellation is to take Dirichlet boundary conditions $A(x = \pm L/2, t) = e^{\pm i \frac{gL}{2} t}$ at the boundaries of the interval $[-L/2, L/2]$. The symmetries $\text{Re}[A(x)] = \text{Re}[A(-x)]$ and $\text{Im}[A(x)] = -\text{Im}[A(-x)]$ allow us to double the resolution (see End Matter) and impose $\text{Im}[A(0)] = 0$. The average frequency at each spatial point shown in Figs. 2b,c confirms the presence of extended regions of synchronization. Note that the equality of average frequencies ensures that phases of oscillators in a plateau vary in time with the same dominant term but may not keep a fixed phase difference (strict phase locking) [2].

The simplest example of parcellation has two plateaus symmetric around the origin, locked at the boundary frequencies $\mp Lg/2$, as shown in Fig. 2c. The jump between the two plateaus dictates the characteristic time $2\pi/gL$ for accumulation of phase differences and amplitude modulation. When the phases in the two plateaus reach $-\pi$ and $+\pi$, a defect appears at $x = 0$. The amplitude oscillates and reaches $A = 0$ at the formation of the defect, when the phase is undefined [2], the 2π difference is reset and the process restarts (see Movie 1 in Ref. [13]). To address amplitude modulation, we decompose $A(x, t) = a(x, t)e^{i\varphi(x, t)}$ and rewrite Eq. (1) as:

$$\partial_t a(x, t) = ra(1 - a^2) - Da(\nabla\varphi)^2 + D\Delta a, \quad (2)$$

$$\partial_t \varphi(x, t) = gx + 2D(\nabla \ln a)(\nabla\varphi) + D\Delta\varphi, \quad (3)$$

to identify $-Da(\nabla\varphi)^2$ as responsible for damping a as $|\nabla\varphi|$ increases, eventually driving $a = 0$ at the defect.

An estimate of the spatial extension of amplitude modulation is calculated using a WKB expansion of a field profile with two plateaus, as shown in Fig. 2c. WKB is the classical method for small diffusion limits [27]. Three

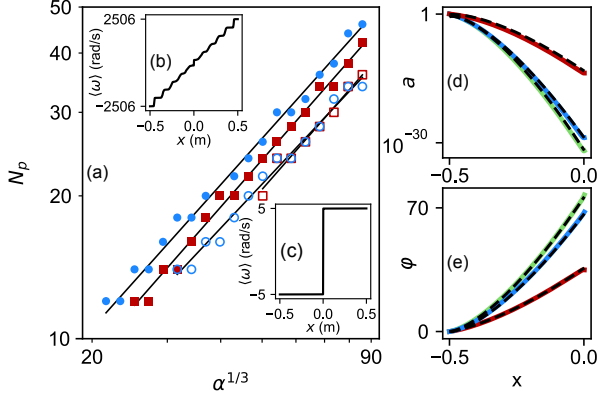


FIG. 2. (Color online) Descriptive properties of plateaus. Panel (a) shows the number of plateaus N_p vs $\alpha^{1/3}$ for Dirichlet (circles) and Neumann (squares) boundary conditions for $\beta = 10^{-2}$ (empty symbols) and 10^{-4} (full symbols); the insets show plateaus for Dirichlet boundary conditions with $L = 1$, $\beta = 10^{-4}$ and (b) $\alpha^{1/3} = 21.56$ or (c) $\alpha^{1/3} = 2.71$. Panels (d) and (e) illustrate amplitude and phase for $\alpha = 4 \times 10^4$ and $\beta = 1$ (red); $\alpha = 2 \times 10^5$ and $\beta = 10$ (green); $\alpha = 1.6 \times 10^5$ and $\beta = 1000$ (blue). The agreement of our WKB prediction (black dashed lines) in the half-interval $[-L/2, 0]$ confirms its validity for large α and moderate/large β .

non-dimensional numbers will be useful to understand the dynamics of Eq. (1):

$$\alpha \equiv \frac{L^3 |g|}{D}; \quad \beta \equiv \frac{Dg^2}{r^3}; \quad \gamma \equiv (\beta \alpha^4)^{\frac{1}{3}} = \frac{L^4 g^2}{rD}. \quad (4)$$

The first yields an estimate of the ratio between the gradient and the diffusive terms, with $\alpha \gg 1$ corresponding to the small diffusion limit. Movie 1 in [13] shows that the field can be reduced to a quasi-static profile with an oscillatory region around $x = 0$ (location of the defect) that shrinks as $|g|$ grows. We found that the WKB profile vs $\tilde{x} \equiv x + L/2$ in the bulk of the left plateau for large α and β reads (see Figs. 2d,e and End Matter):

$$A \propto \frac{e^{-\frac{itgL}{2} - \sqrt{\frac{2}{9}}(1 - i \operatorname{sgn}(g))\left(\frac{\tilde{x}}{\ell_p}\right)^{3/2}}}{\tilde{x}^{1/4}}; \quad \ell_p \equiv \left(\frac{D}{|g|}\right)^{1/3}. \quad (5)$$

Eq. (5) is generalized to moderate β 's in [13].

The length-scale ℓ_p identified by WKB Eq. (5) plays a key role in understanding the increase of N_p with α in Fig. 2a. Uncoupled oscillators spaced by ℓ accumulate phase differences at a rate $|g|\ell$, reaching differences $\simeq \pi$ over times $\tau_\ell \propto 1/|g|\ell$. Diffusive spatial couplings extend their spatial range as the square-root of time. For two points to be coupled strongly enough to lock, it is necessary that $\ell \propto \sqrt{D}\tau_\ell$. We conclude that the characteristic length of plateaus is ℓ_p and

$$N_p \propto \frac{L}{\ell_p} = \alpha^{1/3}. \quad (6)$$

The scaling (6) is consistent with each point oscillating at its own frequency ($\ell_p \rightarrow 0$) in the uncoupled $D \rightarrow 0$

limit and it holds for different boundary conditions, as shown in Fig. 2a. The range of validity of the scaling law (6) depends on β in Eq. (4), which can be recast as $\beta = (|g|\ell_p/r)^3$. As β increases for a fixed large α (or as α decreases), N_p reduces, as confirmed in a limited range in Fig. 2a, and more globally in the (α, β) phase-space plots of Fig. 4 in Ref. [13]. Eventually, the minimum number of plateaus obtains (as in Fig. 2c for small β yet moderate α), the scaling (6) breaks down and boundary conditions matter. The strongest synchrony for Dirichlet boundary conditions has $N_p = 2$; the subtler case of Neumann (no-flux) boundary conditions is considered next.

No flux entails $\nabla A(\pm L/2) = 0$. Plateaus are observed again and, if $N_p \gg 1$, the scaling (6) still holds, demonstrating its generality (see Fig. 2a). At low N_p , the two boundary conditions differ and it appears a new state with the whole interval phase-locked, which is impossible for our Dirichlet setting. Ref. [17] demonstrated locking at large D , and that the corresponding amplitude decreases with $|g|$ and eventually vanishes, i.e., oscillator death with a stable $A = 0$ state is observed [21–23].

Our next goal is to build on these results by studying the linear and nonlinear evolution of the dead $A = 0$ and the locked states. In the linear regime, $|A| \ll 1$, the GL Eq. (1) reduces to

$$\partial_\tau A = \partial_\zeta^2 A + (r' + i\alpha\zeta)A; \quad \zeta \equiv x/L, \quad \tau \equiv Dt/L^2, \quad (7)$$

where $r' \equiv rL^2/D$. Eq. (7) for $r' = 0$ was introduced by Bloch [28] and Torrey [29] for nuclear magnetic resonance based on the following physics. A pulse \mathbf{B}_\perp oscillating at the Larmor frequency ω_L is applied orthogonally to an aligning magnetic field \mathbf{B} . Slowly-varying \mathbf{B} 's are approximated by a gradient, and the linear dependence inherited by ω_L brings in the ζ term in Eq. (7); diffusion accounts for transfer of magnetization in non-homogeneous conditions. Dephasing and diffusion lead to relaxation of the transverse magnetization in the Bloch-Torrey equation, and the decay in time of its eigenmodes [30].

The spectrum of the linear Bloch-Torrey equation is non-trivial, though, as the operator on the right-hand side of Eq. (7) is non-Hermitian. In particular, such operators often feature spectral branch points where two eigenmodes fuse [31]; Figs. 3a,b shows that is the case for the Bloch-Torrey operator [30]. For $\alpha = 0$, all eigenvalues are real as the operator is Hermitian. As α increases, pairs of branches interconnect at branch points for successive values α_p . For $\alpha > \alpha_p$ the corresponding pair of eigenvalues are complex conjugate, with the first branching at $\alpha_1 \approx 18.1$ [30] (see End Matter for details).

Eigenvalues λ_n of the linearized GL Eq. (7) are read from the eigenvalues σ_n 's of the Bloch-Torrey equation ($r' = 0$) by the shift $\lambda_n = \sigma_n + r'$ (see End Matter). While the σ 's have negative real part, the shift makes λ_n 's positive for $r' > -\operatorname{Re}[\sigma_n]$. Fig. 3c illustrates the instabilities expected at small β 's, where the unstable drive

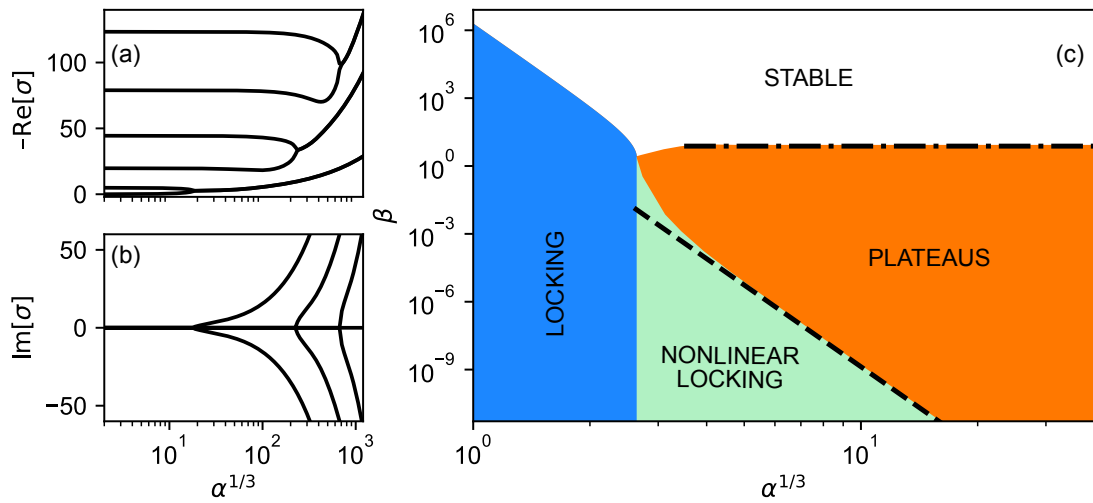


FIG. 3. Eigenvalue spectra and phase space portrait. Panels (a)-(b) report the opposite of the real and the imaginary part of the first six eigenvalues σ_n vs $\alpha^{1/3}$ for the Bloch-Torrey Eq. (7) (ordered by their real part). The imaginary part vanishes before the branching point while two complex conjugate eigenvalues per branch are present afterwards. (c) Phase space portrait. Stable: all eigenvalues have negative real part. Locking: all eigenvalues are real and at least one has positive real part. A locked state is observed in the nonlinear regime [17]. Nonlinear Locking: locking is observed in the nonlinear regime in spite of one or more complex pairs of eigenvalues (linear precursors of plateaus) being present. Plateaus: at least a complex pair of eigenvalues is present and the nonlinear regime features multiple plateaus; the dashed line is the asymptotics $\beta = \gamma_c^3 \alpha^{-4}$ for the critical curve separating locking from multiple plateaus, with the constant γ_c predicted by Eq. (12); the dashed dotted line is the prediction obtained in [30] for a semi-infinite domain (see [13] for details).

r is large (see Eq. (4)). The first pair of complex eigenvalues $\lambda_1^R \pm i\lambda_1^I$ appears at the aforementioned threshold α_1 . In the End Matter we show that the appearance of pairs is associated with precursors of defects, i.e., strong amplitude modulation around $x = 0$ with a period $2\pi/|\lambda_1^I|$.

In the linear regime and $\lambda_1^R < 0$, oscillator death takes place. For $\lambda_1^R > 0$, exponential amplification takes place

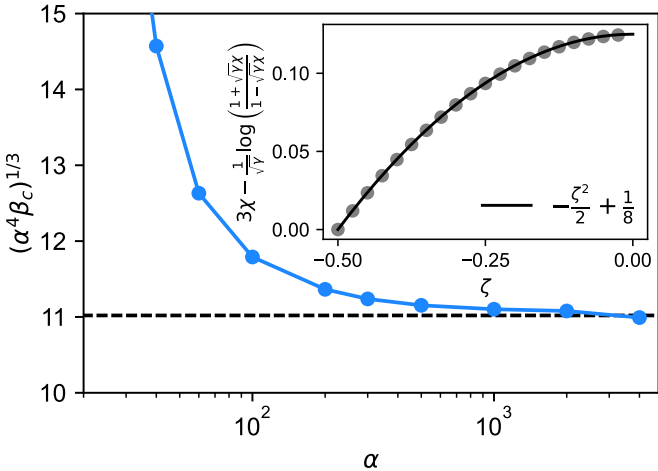


FIG. 4. Nonlinear phase-locking. The critical curve $\alpha^{4/3} \beta_c^{1/3}$ vs α that separates nonlinear locking from multiple plateaus. Convergence to γ_c (dashed line) agrees with our prediction Eq. (12). Inset: The l.h.s. of Eq. (11) vs the rescaled space variable ζ (grey circles) obtained from simulations for $\alpha = 2000$, $\beta = 8.49 \times 10^{-11}$ and our prediction (solid line) Eq. (11).

and nonlinear effects become relevant. The phase diagram is summarized in Fig. 3c. For small α 's, diffusion couples the whole interval and a phase-locked state is observed [17]. As α increases, the range of diffusion shrinks, and the locked state breaks up into multiple plateaus.

While the break up in multiple plateaus was reported in [17], it was concluded that “The transition from locking to plateaus remains obscure”, and the problem remained open. To solve it, we note that Fig. 3c highlights the necessity of nonlinear effects as the transition does not occur at α_1 , as in the linear regime. Specifically, inspection of the critical curve suggests its scaling $\beta_c(\alpha) \propto \alpha^{-4}$, which is the reason we introduced γ in Eq. (4). Locking occurs for $\gamma < \gamma_c$ and the critical values asymptote to $\gamma_c \simeq 11.02$ at large α 's (see Fig. 4).

The above hints are captured and used to understand the transition as follows. Eqs. (2) and (3) are conveniently non-dimensionalized as

$$\partial_\tau a = \alpha^2 a \left[\frac{1 - a^2}{\gamma} - (\varphi')^2 \right] + a'', \quad (8)$$

$$\partial_\tau \varphi = \zeta + 2(\log a)' \varphi' + \varphi'', \quad (9)$$

where we have rescaled space and time as in Eq. (7), and primes denote ζ -derivatives. For large α 's, we neglect the diffusive term in Eq. (8) and assume stationarity to obtain $a \simeq \sqrt{1 - \gamma \varphi'^2}$. Inserting it into Eq. (9), we derive

$$\partial_\tau \varphi = \zeta + \varphi'' \frac{1 - 3\gamma \varphi'^2}{1 - \gamma \varphi'^2}, \quad (10)$$

which shows that nonlinearities renormalize the diffusivity. For $3\gamma\varphi'^2 > 1$, the diffusivity turns negative and an instability is triggered. To localize it, note that $\varphi'(-1/2) = 0$ (no flux) and, if the system is stable, Eq. (10) implies $\varphi'' \propto -\zeta$. It follows that the maximum of φ' , where the negative-diffusivity instability is triggered, occurs at $\zeta = 0$. Its threshold is calculated by considering the stationary Eq. (10): $\chi' \frac{1-3\gamma\chi^2}{1-\gamma\chi^2} = -\zeta$ for $\varphi' \equiv \chi$. Integrating it between $-1/2$ and ζ , we obtain

$$3\chi - \frac{1}{\sqrt{\gamma}} \log \left(\frac{1 + \sqrt{\gamma}\chi}{1 - \sqrt{\gamma}\chi} \right) = -\frac{\zeta^2}{2} + \frac{1}{8}. \quad (11)$$

The critical threshold γ_c is finally derived by requesting $3\gamma_c\chi(0)^2 = 1$, which yields

$$\gamma_c = \left[8 \left(\sqrt{3} - \log \left(\frac{1 + \sqrt{3}}{1 - \sqrt{3}} \right) \right) \right]^2 \simeq 11.027, \quad (12)$$

in excellent agreement with numerics, as shown in Fig. 4. Once the threshold is passed, φ' at the origin grows rapidly, which will squash the amplitude following $a = \sqrt{1 - \gamma\varphi'^2}$. The final stages of the process involve time-dependent effects; it is still interesting to note that the renormalized diffusivity in Eq. (10) diverges when $a = \sqrt{1 - \gamma\varphi'^2} = 0$, i.e., at the formation of the defect.

Our last step is to challenge the GL model to reproduce peristalsis data in Fig. 1. While “waxing and waning” and parcellation are easily captured, having the plateaus above the gradient at the corresponding spatial location is not captured by Eq. (1). However, as we noted, a gradient breaks parity and an additional term $V\nabla A$ is possible in Eq. (1), which represents advection to the right/left depending on the sign of V . Its effects will be detailed elsewhere; the bottomline is that our results still apply but plateaus are advectively displaced and may thus be raised/lowered with respect to their Eulerian natural frequency counterparts. This allows us to reproduce all the features of experimental data as in Fig. 1.

In conclusion, we have characterized the dynamics that leads to parcellation in non-homogeneous oscillatory systems. While our analysis specifically applies to a gradient of natural frequencies, as occurs in peristalsis, we expect that similar considerations apply to forced cases; see Ref. [32] for forced GL. This is likely the case of vasomotion, where neural stimulation acts as a drive for the oscillations of arteriole vessels [9, 10]. Quantitative aspects of the neurovascular coupling remain mysterious, and will benefit from additional experiments. It would, in particular, be ideal to transiently shut down the neuronal activity and assess the undriven vasomotor dynamics. That will provide a sense of the elements that lead to the locking effects recently reported in Ref. [11] and inform their modeling along the lines we presented here.

END MATTER

Numerical simulations. Eq. (1) was integrated by a finite-difference scheme with fourth-order discretization of the Laplacian. We simulated half of the spatial interval and imposed symmetry conditions (Re/Im[A] even/odd) at $x = 0$. $N = 601$ collocation points were used and the ratio of the time step Δt to the smallest natural period satisfied $\frac{gL}{2\pi}\Delta t < 10^{-2}$. Data analysis was performed in the stationary regime eventually reached in simulations.

Clusters identification. We identified plateaus by the clustering algorithm OPTICS [33]. Its input is the matrix $R_{ij} = \frac{1}{T} \sum_{t=0}^T |e^{i(\phi_i(t) - \phi_j(t))}|$ that measures the T -averaged coherence of the phases $\phi_{i,j}(t)$ at positions i, j . Fig. 2 in [13] shows a typical instance of R . Three reasons motivated our OPTICS choice. First, it uses soft clustering, which leaves outliers (often corresponding to defects in our case) unclassified. Second, it is density-based, which is handy when the degree of synchronization is not uniform. Indeed, plateaus are not always “clean”, i.e., with sharp edges and vanishing frequency differences across them (see [13, 25]). Namely, extended plateaus alternating with smaller ones and/or unlocked regions may be observed (see Fig. 1 in [13]). Third, the algorithm provides a systematic method to determine the number of clusters, which was important to identify the scaling (6).

WKB expansion. We consider Eq. (1) for Dirichlet boundary conditions and locking at $\mp gL/2$ of two parcels symmetric around $x = 0$, as in Fig. 2c. We pose $A \equiv \tilde{A}e^{-igL/2t}$ in the left region $-L/2 \leq x \leq 0$, and focus on the bulk of the plateau where $|\tilde{A}| \ll 1$, i.e., away from $-L/2$ and the origin. Movie 1 in Ref. [13] suggests that the bulk profile of \tilde{A} tends to become static and the unlocked region that hosts the defect at $x = 0$ shrinks as g increases. Eq. (1) in the bulk reduces then to

$$0 \simeq \frac{ig(x + \frac{L}{2})}{D} \tilde{A} + \Delta \tilde{A}, \quad (13)$$

where we neglected for simplicity the r term with respect to the gradient. The general case is detailed in [13].

The WKB method poses $\tilde{A} = e^\psi$, and expands $\psi = \psi_0 + \psi_1 + \dots$ with the condition $\psi'' \ll \psi'^2$ [27]. The resulting equations are

$$(\psi'_0)^2 \simeq -\frac{ig(x + \frac{L}{2})}{D}, \quad \psi'_1 \simeq \left(-\frac{1}{2} \log \psi'_0 \right)', \quad (14)$$

whence Eq. (5) follows. The condition $\psi'' \ll \psi'^2$ requires $(x + \frac{L}{2}) \gg \ell_p = (D/|g|)^{1/3}$. The left-hand side being $\sim L$, it follows $\alpha \gg 1$. Neglecting r with respect to gx in Eq. (13) entails $r \ll |g|\ell_p$, i.e., $\beta \gg 1$ [13].

Spectrum of the linearized GL equation. Plugging the ansatz $A(\zeta, \tau) = \rho(\zeta)e^{\lambda\tau}$ in Eq. (7), we obtain

$$(r' - \lambda + i\alpha\zeta + \Delta)\rho = 0, \quad (15)$$

with $\nabla\rho(\zeta = \pm 1/2) = 0$. Eq. (15) shows that its eigenvalues λ_n are related to the σ_n 's of the Bloch-Torrey equation ($r' = 0$) by the shift $\lambda_n = \sigma_n + r'$. We computed the σ_n 's numerically by using the ZGEEV function in LAPACK [34], which returns eigenvalues ordered by their real part. To span the α range, we fixed $D = 0.5$, $L = 1$, and varied $g = 10^{0.1n}$, with the integer $n \in [0, 60]$. Our numerics is consistent with Ref. [30] with the change that $L = 2$ instead of our $L = 1$. To perform the verification, we re-derived results in [30] as detailed in [13].

Precursors of defects. We consider the linearized GL Eq. (7) in the regime where the first branching occurred (see Fig. 3a,b). We show that branching is associated to strong modulation of the amplitude (precursor of defects) around the origin $x = 0$. The pair of branched eigenvalues with the largest real part is denoted $\lambda_1^R \pm i\lambda_1^I$. The dominant asymptotics of the field A at large times is

$$A(x, t) \propto e^{\lambda_1^R t} \left[\rho_+(x) e^{i\lambda_1^I t} + \rho_-(x) e^{-i\lambda_1^I t} \right], \quad (16)$$

where ρ_{\pm} are the eigenmodes. Eq. (15) for the eigenmodes is symmetric under $\lambda^I \leftrightarrow -\lambda^I$, $x \leftrightarrow -x$, $\rho \leftrightarrow \rho^*$, which implies $\rho_-(x) = \rho_+^*(-x)$ [30]. The expression (16) at the origin reduces then to $2e^{\lambda_1^R t} |\rho_+(0)| \cos(\lambda_1^I t + \arg(\rho_+(0)))$, which vanishes periodically with period $2\pi/|\lambda_1^I|$.

We thank Jacob Duckworth, Vladimir Matchkov, and Marcelo Rozenberg for relevant discussions. This work was supported by the NIH U19 Cooperative Agreement Grant (U19 NS123717).

- [1] Y. Kuramoto. *Chemical Oscillations, Waves, and Turbulence* (Springer Series in Synergetics, Vol. 19, 1984).
- [2] A. Pikovsky, M. Rosenblum, and J. Kurths. *Synchronization. A Universal Concept in Nonlinear Sciences* (Cambridge University Press, 2001).
- [3] S. Strogatz. *Sync: The Emerging Science of Spontaneous Order* (Penguin, 2004).
- [4] J. Buck, and E. Buck. *Nature* **211**, 562-564 (1966).
- [5] R. Sarfati, J.C. Hayes, E. Sarfati, and O. Peleg. *J. R. Soc. Interface* **17**, 20200179 (2020).
- [6] S. Grillner, and A. El Manira. *Physiol. Rev* **100**, 271-320 (2020).
- [7] P.J. Muller, F. Chavane, J. Reynolds, and T.J. Sejnowski. *Nat. Rev. Neurosci.* **107**, 782-804 (2018).
- [8] B. Ermentrout, and D. Kleinfeld. *Neuron* **29**, 33-44 (2001).
- [9] R.E. Haddock, and C.E. Hill. *J. Physiol.* **566**, 645-656 (2005).
- [10] P.J. Drew, C. Mateo, K. Turner, X. Yu, and D. Kleinfeld. *Neuron* **107**, 782-804 (2020).
- [11] T. Broggini, J. Duckworth, X. Ji, R. Liu, X. Xia, P. Machler, I. Shaked, L.P. Munting, S. Iyengar, M. Kotlikoff, S.J. van Veluw, M. Vergassola, G. Mishne, and D. Kleinfeld. *Neuron* **112**, 1-19 (2024).

- [12] A.T. Winfree. *The Geometry of Biological Time* (Springer-Verlag, New York, 2nd Ed, 2001).
- [13] See Supplemental Material for numerical methods, data analysis, asymptotic WKB calculations, and re-derivation of results in [30]. It includes Refs. [35-41].
- [14] N.E. Diamant, and A. Bortoff. *Am. J. Physiol.* **216**, 301-307 (1969).
- [15] S.P. Parsons, and J.D. Huizinga. *Sci. Rep.* **10**, 15099 (2020).
- [16] G.B. Ermentrout, and N. Kopell. *Siam. J. Math. Anal.* **15**, 215-237 (1984).
- [17] G.B. Ermentrout, and W.C. Troy. *Siam. J. Appl. Math.* **46**, 359-367 (1986).
- [18] G.V. Osipov, and M.M. Sushchik. *Phys. Rev. E* **58**, 7198 (1998).
- [19] K.O. Menzel, O. Arp, and A. Piel. *Phys. Rev. E* **84**, 016405 (2011).
- [20] K.O. Menzel, O. Arp, and A. Piel. *Phys. Rev. E* **83**, 016402 (2011).
- [21] G.B. Ermentrout. *Physica D* **41**, 219-231 (1990).
- [22] D.V. Ramana Reddy, A. Sen, and G.L. Johnston. *Phys. Rev. Lett.* **85**, 3381 (2000).
- [23] I. Ozden, S. Venkataramani, M.A. Long, B.W. Connors, and A.V. Nurmikko. *Phys. Rev. Lett.* **93**, 158102 (2004).
- [24] I.S. Aranson, and L. Kramer. *Rev. Mod. Phys.* **74**, 99-143 (2002).
- [25] A.A. Akopov, T.E. Vadivasova, V.V. Astakhov, and D.D. Matyushkin. *Tech. Phys. Lett.* **29**, 629-631 (2003).
- [26] V.S. Anishchenko, T.E. Vadivasova, G.A. Okrokvertskhov, A.A. Akopov, and G.I. Strelkova. *International Journal of Bifurcation and Chaos* **15**, 3661-3673 (2005).
- [27] C.M. Bender, and S.A. Orszag. *Advanced Mathematical Methods for Scientists and Engineers. Asymptotic Methods and Perturbation Theory*. (Springer, 1999).
- [28] F. Bloch. *Phys. Rev.* **70**, 460 (1946).
- [29] H.C. Torrey. *Phys. Rev.* **104**, 563 (1956).
- [30] S.D. Stoller, W. Happer, and F.J. Dyson. *Phys. Rev. A* **44**, 7459 (1991).
- [31] N. Moutal, and D.S. Grebenkov. *J. Phys. A* **55**, 455201 (2022).
- [32] A. Golden, A.E. Sgro, and P. Mehta. *Phys. Rev. E* **103**, 042211 (2021).
- [33] H.P. Kriegel, P. Kröger, J. Sander, and J. Zimek. *Wiley Interdisciplinary Reviews: Data Mining and Knowledge Discovery* **1**, 231-240 (2011).
- [34] E. Anderson, Z. Bai, C. Bischof, S. Blackford, J. Dongarra, J. Du Croz, A. Greenbaum, S. Hammarling, A. McKenney, and D. Sorensen. *LAPACK Users' Guide* (SIAM, 1999).
- [35] A. Rohatgi. *WebPlotDigitizer* at <https://automeris.io>. Version 5.2 (2024).
- [36] G.V. Osipov, and M.M. Sushchik. *IEEE Trans. Circ. Sys. I: Fund. Theor. Appl.* **44**, 1006-1010 (1997).
- [37] V.S. Anishchenko, A.A. Akopov, T.E. Vadivasova, and G.I. Strelkova. *New J. Phys.* **8**, 84-94 (2006).
- [38] M. Ankerst, M.M. Breunig, H.-P. Kriegel, and J. Sander. *SIGMOD Rec.* **28**, 49-60 (1999).
- [39] H. Daido. *Prog. Theor. Phys.* **102**, 197-202 (1999).
- [40] O. Vallée, and M. Soares. *Airy Functions and Applications to Physics* (World Scientific, 2004).
- [41] M. Abramowitz, and I.A. Stegun. *Handbook of Mathematical Functions with Formulas, Graphs, and Mathematical Tables* (Dover, 1964).